High-Flux Neutron Generator Based on Laser-Driven Collisionless Shock Acceleration

Y. L. Yao[1,*], S. K. He[2,*], Z. Lei[1,*], T. Ye,[3] Y. Xie,[1] Z. G. Deng,[2] B. Cui,[2] W. Qi,[2] L. Yang,[2]
S. P. Zhu,[3] X. T. He,[3] W. M. Zhou[2,†] and B. Qiao[1,4,‡]

[1]*Center for Applied Physics and Technology, HEDPS and State Key Laboratory of Nuclear Physics and Technology,*
School of Physics, Peking University, Beijing 100871, China
[2]*Science and Technology on Plasma Physics Laboratory, Research Center of Laser Fusion,*
China Academy of Engineering Physics (CAEP), Mianyang 621900, China
[3]*Institute of Applied Physics and Computational Mathematics, Beijing 100094, China*
[4]*Frontiers Science Center for Nano-optoelectronic, Peking University, Beijing 100094, China*

A novel compact high-flux neutron generator with a pitcher-catcher configuration based on laser-driven collisionless shock acceleration (CSA) is proposed and experimentally verified. Different from those that previously relied on target normal sheath acceleration (TNSA), CSA in nature favors not only acceleration of deuterons (instead of hydrogen contaminants) but also increasing of the number of deuterons in the high-energy range, therefore having great advantages for production of high-flux neutron source. The proof-of-principle experiment has observed a typical CSA plateau feature from 2 to 6 MeV in deuteron energy spectrum and measured a forward neutron flux with yield 6.6×10^7 n/sr from the LiF catcher target, an order of magnitude higher than the compared TNSA case, where the laser intensity is 10^{19} W/cm^2. Self-consistent simulations have reproduced the experimental results and predicted that a high-flux forward neutron source with yield up to 5×10^{10} n/sr can be obtained when laser intensity increases to 10^{21} W/cm^2 under the same laser energy.

Neutrons with electric neutrality have the power to probe and modify material properties or excite nuclear reactions in a unique way that cannot be achieved using other radiations. This enables neutrons to be applied in a wide range of fields from physics [1], material science [2], and security service [3], to medical science [4]. All the applications require a high-flux neutron generator that not only creates large amounts of neutrons but also maximizes the number of neutrons delivered through a specific area. Historically, nuclear reactors and accelerator-based spallation sources have been primarily used. Unfortunately, these facilities not only take up a large space but also are expensive to build and maintain [5–7].

A laser-driven neutron source with a pitcher-catcher configuration provides an attractive alternative with low cost and compact size, where the high-energy ions accelerated from laser-irradiated targets (the pitcher) are used to drive nuclear reactions in a converter material (the catcher) for neutron productions. Because of having the high cross sections, deuteron-induced reactions such as ^{7}Li(d, xn), ^{9}Be(d, xn), and D$(d, n)^3$He are generally applied. So far, the most-investigated scheme is based on target normal sheath acceleration (TNSA). However, two major drawbacks exist with this scheme. On the one hand, TNSA preferentially accelerates the hydrogen contaminants that have the highest charge-to-mass ratio so that all present experiments suffer from low conversion efficiency for

deuteron acceleration, although several complex techniques [8–12] have been tried to remove contaminants. On the other hand, ions accelerated by TNSA [13–17] and even enhanced TNSA (named break-out afterburner [18,19]) exhibit exponentially decaying energy spectra, where the ion number in the high-energy range is rather low. Both of these prevent production of high-flux neutrons relying on TNSA.

In this Letter, we propose a novel scheme for production of a high-flux neutron source, where laser-driven collisionless shock acceleration (CSA) [20–25] is applied. In CSA, the laser launches an electrostatic shock wave in near-critical plasmas, which, with the sharp, strong electrostatic field, can continuously reflect and accelerate the plasma ions to high energy during propagation, irrespective of charge-to-mass ratios. Therefore, comparing with TNSA, CSA has great advantages not only for acceleration of deuterons but also for increasing the number of deuterons in the high-energy range, which eventually results in production of high-flux neutrons via nuclear reactions in the catcher. To verify this idea, we carry out the proof-of-principle experiment by using a subtle target design for formation of the near-critical plasma with a proper density profile. A typical CSA plateau feature from 2 to 6 MeV in deuteron energy spectrum is observed with laser intensity 10^{19} W/cm^2 and a forward neutron flux with yield 6.6×10^7 n/sr (flux $> 5 \times 10^7$ n/cm^2) after the LiF target is

025101-1
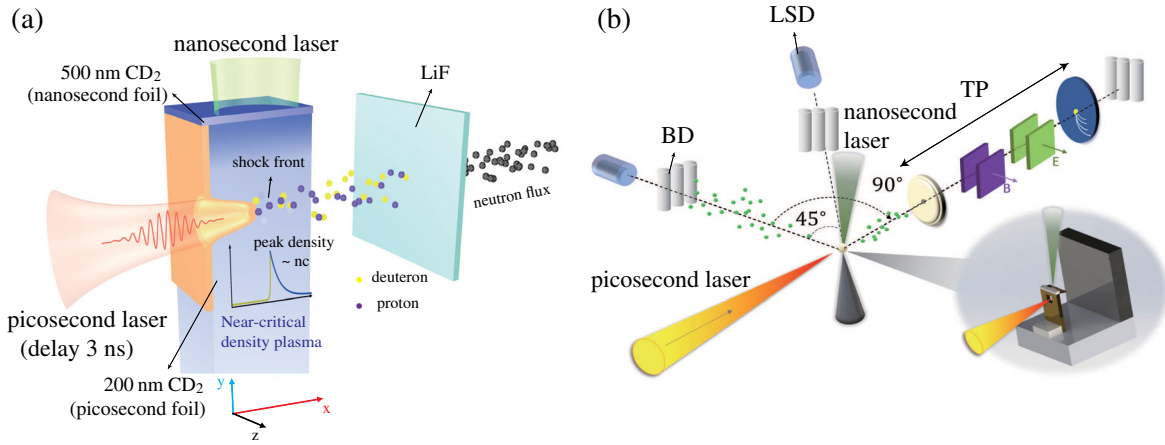
FIG. 1. Schematic view of the experiment. (a) Experimental setup. The pitcher target consists of two nanometer CD_2 foils perpendicular to each other, which are irradiated by, respectively, nanosecond and picosecond lasers (called "nanosecond foil" and "picosecond foil"), and the catcher LiF converter block is placed 10 cm away. Ions including both deuterons and protons are firstly accelerated by picosecond laser-driven CSA in the near-critical plasma (formed from expansions of both foils) and then are deposited into LiF converter for neutron production. (b) Diagnostics setup. A Thomson parabola (TP) spectrometer is placed 15 cm away (with solid angle 1.4×10^{-6} sr) to detect the forward ion energy spectra. Three groups of bubble detectors (BDs) are placed at, respectively, $0°$ (14 cm away), $45°$ (10.3 cm), and $90°$ (17.5 cm) relative to the forward direction to measure the absolute neutron yields. Two liquid scintillation detectors (LSDs) are placed at $45°$ and $90°$ to measure the neutron energy spectra. The LSDs are shielded by a 20-cm-thick lead brick so that x rays are absorbed. The LSDs are calibrated with two energy points, 2.45 and 14.1 MeV, using a compact dense plasma focus neutron source and a 400 keV electrostatic accelerator neutron source [27].

measured, which is an order of magnitude higher in either yield or flux than those obtained in the compared TNSA shots. The experimental results are reproduced by the self-consistent simulations with a combination of radiation magnetohydrodynamic (RMHD), particle-in-cell (PIC), and Monte Carlo (MC) methods. The simulations also predict a high-flux neutron source with yield 5×10^{10} n/sr can be obtained at 10^{21} W/cm^2, more than an order of magnitude higher than the current record [18] under the same laser energies.

The experiments are carried out at XingGuang-III (XG-III) laser facility [26], which can simultaneously output femtosecond, picosecond, and nanosecond pulses with wavelengths 800, 1053, and 527 nm, respectively. We use picosecond and nanosecond pulses with output energies and pulse durations of, respectively, 80 J/0.8 ps (intensity 1×10^{19} W/cm^2) and 150 J/2.0 ns (6×10^{13} W/cm^2). Figure 1(a) shows a schematic view of our experimental setup. The pitcher target consists of two separate CD_2 foils perpendicular to each other, where the horizontal one at the top with thickness 500 nm is ablated by nanosecond pulse (called a "nanosecond foil"), and the vertical one with thickness 200 nm is irradiated by picosecond pulse (called "picosecond foil") with a delay of 3 ns. The catcher at 10 cm away is a 2-cm-thick LiF block, where nuclear reactions $^7\mathrm{Li}(d, xn)$ and $^7\mathrm{Li}(p, xn)$ are expected. Different from those using a single foil irradiated by two laser beams with a delay [23,24], here the tailored near-critical plasma density profile required for launching CSA, i.e., an exponentially decreasing density profile, is designed to be

formed by two parts. One is from vertically downward expansion of the nanosecond foil that is ablated by nanosecond pulse, and the other is from rear-side expansion of the picosecond foil due to both the indirect heating conducted from nanosecond foil and the impact of hot plasma flow expanded from nanosecond foil. Such a novel target design allows us to easily adjust the parameters of two foils and lasers so that the optimal tailored plasma density profile for CSA is obtained. CSA is driven by a picosecond laser through such near-critical plasmas. The experimental shots for the case without nanosecond laser ablation are also performed for comparison, where TNSA dominates. Figure 1(b) shows the diagnostics setup; see details in its caption.

The experimental results are summarized in Fig. 2. We see strong signals for both deuterons (including a small part of C^{6+} that has the same charge-to-mass ratio) and protons on the raw image plate (IP) data of the Thomson parabola (TP) spectrometer for the case with nanosecond laser ablation where CSA dominates [see Fig. 2(a)], whereas the deuteron signal is rather weak for the case without ablation where TNSA dominates [Fig. 2(b)]. The corresponding ion energy spectra parsed from the IP data for both cases are shown in Fig. 2(c). We see for the case with ablation a large number of deuterons are accelerated to high energy, whose energy spectrum exhibits a pronounced plateau feature from 2 to 6 MeV with the maximum up to 8 MeV (the red solid line), and proton contaminants are also accelerated to similar energy per nucleon up to 4 MeV (the purple solid line). This verifies domination of CSA
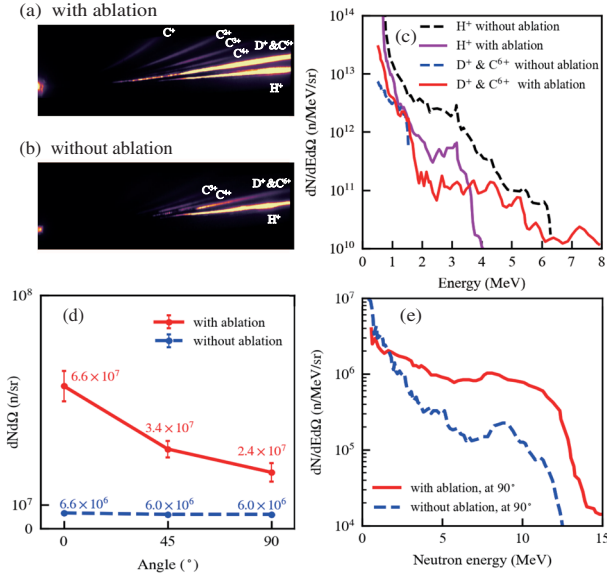
FIG. 2. Experimental results. (a),(b) Raw image plate data of the on-axis Thomson parabola spectrometer for the cases with and without nanosecond laser ablation, respectively. (c) The corresponding ion energy spectra obtained from TP. (d) Neutron yields at 0°, 45°, and 90° for the cases with and without ablation. (e) The corresponding neutron energy spectra.

here. By contrast, for the case without ablation, TNSA dominates and protons are preferentially accelerated to high energy (the black dashed line), whereas deuteron acceleration is inhibited (the blue dashed line). Note that both the maximum energy and particle number of the accelerated protons for the case with ablation (the purple solid line) are much smaller than without ablation (the black dashed line), because the ablation also helps to remove contaminants.

Figure 2(d) shows the neutron yield data from three bubble detectors (BDs). For the CSA case with ablation (see three red dots), since the high-energy deuteron-induced reaction $^7\mathrm{Li}(d, xn)$ dominates, the neutron yield at 0° is much higher than the other two, implying the neutron flux is forward directed, whereas for the compared TNSA case (three blue dots), the neutron yield shows isotropic angular distribution where the $^7\mathrm{Li}(p, xn)$ reaction dominates. More importantly, we see that the forward neutron flux has a high yield 6.6×10^7 n/sr (flux $> 5 \times 10^7$ n/cm^2) in CSA, which is an order of magnitude higher than the compared TNSA case. The neutron energy spectrum obtained from the liquid scintillation detector (LSD) for the CSA case is shown by the red solid line in Fig. 2(e), having also a plateau from 7.5 to 12.5 MeV. Additionally, the maximum neutron energy is much larger than the compared TNSA case. Note that, for the $^7\mathrm{Li}(d, n)^7\mathrm{Be}$ channel, the low-energy deuterons ($\sim$1 MeV) have probabilities of producing high-energy neutrons (around 8 MeV), which is the reason that the spectrum in the TNSA case [the dashed blue line in Fig. 2(e)] also shows a small bump feature.

To understand the experimental results, we carry out a series of self-consistent simulations that combines RMHD for modeling the tailored near-critical plasma formation, PIC for laser-driven proton and deuteron acceleration, and MC simulations for nuclear reaction and neutron production. The simulation results are summarized in Fig. 3. Density map and on-axis profiles of the near-critical plasma obtained by 2D RMHD simulation using FLASH [28] are shown in Figs. 3(a) and 3(b). As expected, the profile has a steep rising front up to the peak close to the critical density and after that an exponentially decreasing trailing edge. This is exactly what is required for the picosecond laser to launch CSA. Furthermore, we see from Fig. 3(b) that this near-critical plasma profile is rather stable for a long time until 3 ns when picosecond laser propagates through. This clearly verifies that our target design with a separate ablated nanosecond foil is much more advantageous than those previously by direct ablation of the picosecond foil. More details about the RMHD simulation results can be seen in Note 1 of the Supplemental Material [29].

The plasma profile obtained above is applied as the initial conditions for 2D PIC simulations with EPOCH [48]. We assume C^{6+} and d^+ ions dominate at region I and region II in Fig. 3(b) with density ratio $n_{\mathrm{C}^{6+}} : n_{d^+} = 1\!:\!2$, and in region III, due to the presence of proton contaminants, we assume $n_{\mathrm{C}^{6+}} : n_{d^+} : n_{p^+} = 1\!:\!1\!:\!1$. For the TNSA case, due to the limitation in computational resources, we scaled down the picosecond foil parameters by decreasing density to $50n_c$ while increasing thickness to 2 μm to ensure the same areal density as in experiments. The ion density ratio is the same. We also assume a 0.1-μm-thick proton contaminant layer of $50n_c$ at the picosecond foil rear surface. The picosecond laser parameters are chosen exactly the same as those in experiments.

Figure 3(c) plots longitudinal profiles of the deuteron density (dashed lines) and electrostatic field E_x (solid lines) at $t_{\mathrm{ps}} = 1.05$ and 2.65 ps. We see that a collisionless shock wave is launched, where the deuteron density exhibits a sharp jump, inducing steep E_x. This shock wave propagates rather stably until $t_{\mathrm{ps}} = 2.65$ ps much later after the picosecond laser ends. The average temperature of the upstream plasma is $T_e \approx 4.17$ MeV and the shock velocity is $v_s \approx 0.12c$, concluding that the shock Mach number is $\mathrm{M} = v_s/c_s \sim 1.8$, capable of reflecting ions for acceleration [22,49]. This shock wave continuously reflects both deuterons and protons to high energies, as can be seen in Figs. 3(d) and 3(e) for their (x, p_x) phase space distributions.

The final energy spectra of deuterons and protons from PIC simulations are plotted in Fig. 3(f) by solid lines, where two conversion factors are introduced to convert 2D simulation results (particle number f_N and ion energy f_{E_n}) to realistic 3D, so that they can be compared with the experimental results. Considering the simple geometric difference, we give $f_N = N_{3\mathrm{D}}/N_{2\mathrm{D}} = \pi r_0/2h$, where r_0
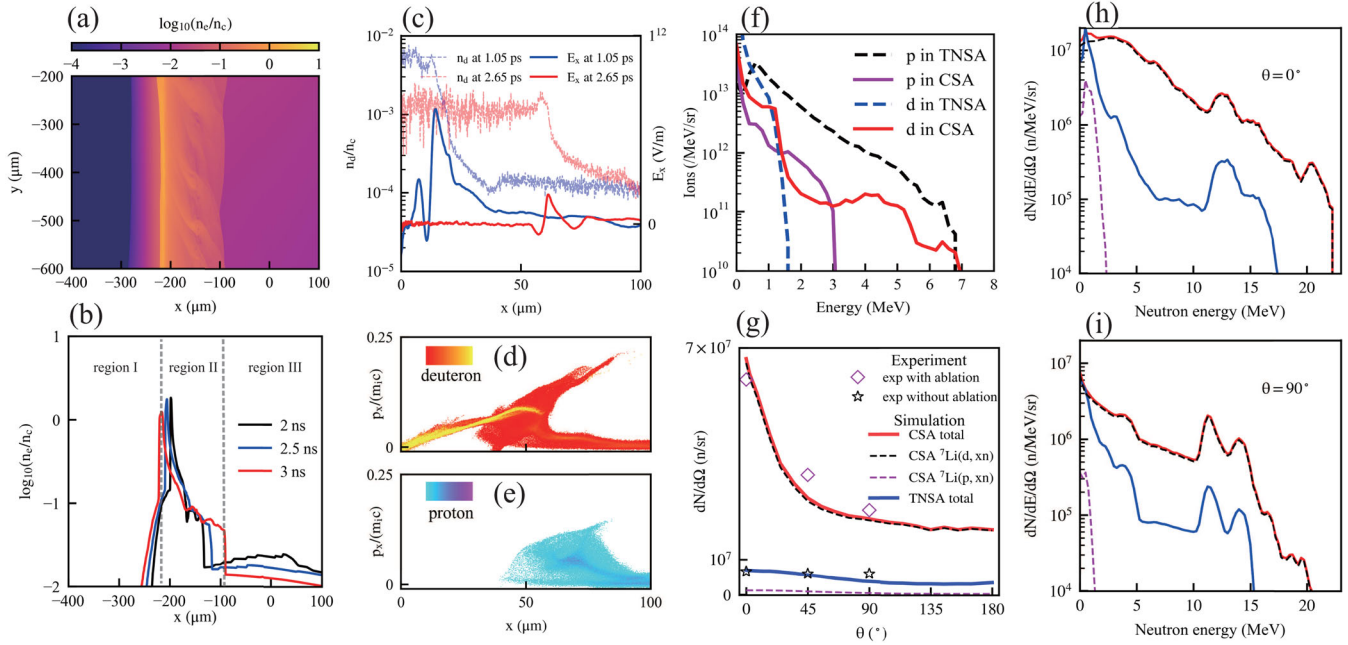
FIG. 3. Self-consistent simulation results. (a),(b) Density map at $t_{ns} = 3$ ns and on-axis profiles at $t_{ns} = 2$, 2.5, and 3 ns of the near-critical plasma obtained from 2D RMHD simulations with same x axis, where t_{ns} is the time after nanosecond laser has arrived at nanosecond foil. Picosecond foil is vertically located at $x = -200$ μm and nanosecond foil is horizontally located at $y = 400$ μm. (c) Longitudinal profiles of the deuteron density (dashed lines) and the electrostatic field E_x (solid lines) at $t = 1.05$ and 2.65 ps obtained from 2D PIC simulations, where t_{ps} is the time after picosecond laser has arrived at picosecond foil. (d),(e) Phase space distributions (x, p_x) for, respectively, deuterons and protons at $t_{ps} = 2.5$ ps for the CSA case obtained from 2D PIC simulations. (f) The corresponding final energy spectra of deuterons and protons obtained from 2D PIC simulations. (g) Angular distributions of the total neutron yield and its contributions, respectively, from (d, xn) and (p, xn) reactions obtained from 3D MC nuclear reaction simulations for the CSA case, in comparison with the experimental results as well as the TNSA cases. (h),(i) The corresponding energy spectra of neutrons at $\theta = 0°$ and $\theta = 90°$, which have the same legends as those in (g).

is the laser focal radius and $h = 1.0$ m is the nonsimulated dimension size assumed in 2D simulations. For the ion energy, we apply the results in Ref. [50] as $f_{E_n} = E_{n,3D}/E_{n,2D} = \sqrt{2/\pi r_0}$. We see that the deuteron energy spectrum also shows a plateau feature from 2 to 6 MeV with particle number of 2×10^{11}, in good agreement with experimental results. Similarly, we see from the dashed blue line in Fig. 3(f) that deuteron acceleration is heavily suppressed in the TNSA case.

Next, the data of the accelerated deuterons and protons from PIC simulations are used as the input for MC simulations of nuclear reactions. A MC code (named MCNRC) is developed, whose details and benchmark can be see in Note 2 of the Supplemental Material [29]. Figure 3(g) plots the angular distributions of the total neutron yield as well as its contributions from, respectively, deuteron ^{7}Li(d, xn) and proton ^{7}Li(p, xn) reactions. We see from the solid red line that the total neutron yields at 0°, 45°, and 90° all agree with the experimental data (see the diamond symbols) and the neutron flux is forward directed. By comparing the black and the purple dashed lines, we conclude the deuteron-induced reaction ^{7}Li(d, xn) dominates, contributing about 98% of the forward neutron yield. The angular distribution of the neutron yield for the TNSA

case is also plotted by the blue solid line, which shows an order of magnitude lower yields and also isotropic angular distribution, because the ^{7}Li(p, xn) reaction dominates there. Figures 3(h) and 3(i) plot the energy spectra of neutrons at, respectively, 0° and 90° for both CSA (red solid line) and TNSA (blue solid line) cases, where the ones at 90° are also in agreement with the experimental result in Fig. 2(e). Moreover, we find that deuterons in the plateau energy range from 2 to 6 MeV, though covering only 6% of the total particle number, contribute more than 50% of the forward neutron yield, further verifying the great advantage of CSA for production of high-energy deuterons.

To show the robustness and advantages of our scheme, we further carry out a series of simulations with laser intensities increased from 10^{19} to 10^{21} W/cm^2 and the corresponding focal radius decreased from 20 to 2.5 μm, where laser energies are kept the same as 80 J. The results are shown in Fig. 4 for, respectively, (a) the forward neutron energy spectra and (b) the forward neutron yields. We see that the maximum neutron energy is greatly enhanced when laser intensity increases, and the forward neutron yield increases linearly with the laser intensity having scaling of $\propto I$, much more superior than that ($\propto I^{1/2}$) in the TNSA scheme. When the laser intensity increases to 10^{21} W/cm^2,
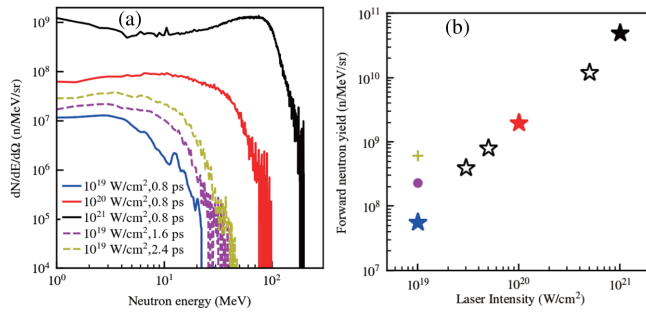
FIG. 4. Simulation results for the proposed scheme with different laser parameters (intensities and pulse durations). (a) Energy spectra of the forward neutron flux at 0° and (b) forward neutron yield at 0°.

the same as that in Ref. [18], a forward neutron yield of 5×10^{10} n/sr is obtained in our CSA scheme, more than an order of magnitude higher than Ref. [18]. More details of the discussions and simulation results are shown in Note 3 of the Supplemental Material [29]. Furthermore, we see that by extending laser pulse durations, the neutron yield is also enhanced [the dashed lines in Fig. 4(a)], because in CSA repeated reflections and accelerations of background ions result in continuous increasing of deuteron number with time, i.e., laser pulse duration.

In conclusion, we have theoretically proposed and experimentally demonstrated a novel method to generate high-flux neutrons, where the laser-driven CSA is realized via a dedicate target design to facilitate the creation of a tailored near-critical-density profile. The obtained forward neutron flux is about one order of magnitude higher than the TNSA. Our Letter paves the way toward compact neutron sources that have important applications in diverse scientific fields.

[*]These authors contributed equally to this work.

[†]Corresponding author.
zhouwm@caep.cn

[‡]Corresponding author.
bqiao@pku.edu.cn

[1] R. Dams, J. A. Robbins, K. Rahn, and J. W. Winchester, Anal. Chem. **42**, 861 (1970).

[2] Y. Nishiyama, J. Sugiyama, H. Chanzy, and P. Langan, J. Am. Chem. Soc. **125**, 14300 (2003).

[3] P. Jung, A. Hishinuma, G. Lucas, and H. Ullmaier, J. Nucl. Mater. **232**, 186 (1996).

[4] R. F. Barth, A. H. Soloway, and R. G. Fairchild, Sci. Am. **263**, 100 (1990).

[5] P. Ageron, Nucl. Instrum. Methods Phys. Res., Sect. A **284**, 197 (1989).

[6] B. Blau, K. N. Clausen, S. Gvasaliya, M. Janoschek, S. Janssen, L. Keller, B. Roessli, J. Schefer, P. Tregenna-Piggott, W. Wagner et al., Neutron News **20**, 5 (2009).

[7] J. Wei, H. Chen, Y. Chen, Y. Chen, Y. Chi, C. Deng, H. Dong, L. Dong, S. Fang, J. Feng et al., Nucl. Instrum. Methods Phys. Res., Sect. A **600**, 10 (2009).

[8] M. Hegelich, S. Karsch, G. Pretzler, D. Habs, K. Witte, W. Guenther, M. Allen, A. Blazevic, J. Fuchs, J. C. Gauthier, M. Geissel, P. Audebert, T. Cowan, and M. Roth, Phys. Rev. Lett. **89**, 085002 (2002).

[9] P. Mckenna, F. Lindau, O. Lundh, D. Carroll, R. Clarke, K. Ledingham, T. McCanny, D. Neely, A. Robinson, L. Robson et al., Plasma Phys. Controlled Fusion **49**, B223 (2007).

[10] M. Allen, P. K. Patel, A. Mackinnon, D. Price, S. Wilks, and E. Morse, Phys. Rev. Lett. **93**, 265004 (2004).

[11] A. Krygier, J. Morrison, S. Kar, H. Ahmed, A. Alejo, R. Clarke, J. Fuchs, A. Green, D. Jung, A. Kleinschmidt et al., Phys. Plasmas **22**, 053102 (2015).

[12] A. Alejo, A. Krygier, H. Ahmed, J. Morrison, R. Clarke, J. Fuchs, A. Green, J. Green, D. Jung, A. Kleinschmidt et al., Plasma Phys. Controlled Fusion **59**, 064004 (2017).

[13] D. P. Higginson, L. Vassura, M. M. Gugiu, P. Antici, M. Borghesi, S. Brauckmann, C. Diouf, A. Green, L. Palumbo, H. Petrascu, S. Sofia, M. Stardubtsev, O. Willi, S. Kar, F. Negoita, and J. Fuchs, Phys. Rev. Lett. **115**, 054802 (2015).

[14] S. Kar, A. Green, H. Ahmed, A. Alejo, A. Robinson, M. Cerchez, R. Clarke, D. Doria, S. Dorkings, J. Fernandez et al., New J. Phys. **18**, 053002 (2016).

[15] L. Willingale, G. Petrov, A. Maksimchuk, J. Davis, R. Freeman, A. Joglekar, T. Matsuoka, C. Murphy, V. Ovchinnikov, A. Thomas et al., Phys. Plasmas **18**, 083106 (2011).

[16] C. Zulick, F. Dollar, V. Chvykov, J. Davis, G. Kalinchenko, A. Maksimchuk, G. Petrov, A. Raymond, A. Thomas, L. Willingale et al., Appl. Phys. Lett. **102**, 124101 (2013).

[17] D. Higginson, J. McNaney, D. Swift, G. Petrov, J. Davis, J. Frenje, L. Jarrott, R. Kodama, K. Lancaster, A. Mackinnon et al., Phys. Plasmas **18**, 100703 (2011).

[18] M. Roth, D. Jung, K. Falk, N. Guler, O. Deppert, M. Devlin, A. Favalli, J. Fernandez, D. Gautier, M. Geissel et al., Phys. Rev. Lett. **110**, 044802 (2013).

[19] A. Kleinschmidt, V. Bagnoud, O. Deppert, A. Favalli, S. Frydrych, J. Hornung, D. Jahn, G. Schaumann, A. Tebartz, F. Wagner et al., Phys. Plasmas **25**, 053101 (2018).

[20] D. Haberberger, S. Tochitsky, F. Fiuza, C. Gong, R. A. Fonseca, L. O. Silva, W. B. Mori, and C. Joshi, Nat. Phys. **8**, 95 (2012).

[21] W. Zhang, B. Qiao, T. Huang, X. Shen, W. You, X. Yan, S. Wu, C. Zhou, and X. He, Phys. Plasmas **23**, 073118 (2016).

[22] F. Fiúza, A. Stockem, E. Boella, R. A. Fonseca, L. O. Silva, D. Haberberger, S. Tochitsky, C. Gong, W. B. Mori, and C. Joshi, Phys. Rev. Lett. **109,** 215001 (2012).

[23] P. Antici, E. Boella, S. Chen, D. Andrews, M. Barberio, J. Böker, F. Cardelli, J. Feugeas, M. Glesser, P. Nicolaï et al., Sci. Rep. **7,** 16463 (2017).

[24] A. Pak, S. Kerr, N. Lemos, A. Link, P. Patel, F. Albert, L. Divol, B. Pollock, D. Haberberger, D. Froula, M. Gauthier, S. H. Glenzer, A. Longman, L. Manzoor, R. Fedosejevs, S. Tochitsky, C. Joshi, and F. Fiuza, Phys. Rev. Accel. Beams **21,** 103401 (2018).

[25] M. Gauthier, A. Levy, E. d'Humières, M. Glesser, B. Albertazzi, C. Beaucourt, J. Breil, S. Chen, V. Dervieux, J. Feugeas et al., Phys. Plasmas **21,** 013102 (2014).

[26] Q. Zhu, K. Zhou, J. Su, N. Xie, X. Huang, X. Zeng, X. Wang, X. Wang, Y. Zuo, D. Jiang et al., Laser Phys. Lett **15,** 015301 (2017).

[27] B. Cui, Z. Fang, Z. Dai, H. Liu, W. Wang, J. Chen, B. Bi, C. Tian, D. Liu, W. Wang et al., Laser Part. Beams **36,** 494 (2018).

[28] B. Fryxell, K. Olson, P. Ricker, F. Timmes, M. Zingale, D. Lamb, P. MacNeice, R. Rosner, J. Truran, and H. Tufo, Astrophys. J. Suppl. Ser. **131,** 273 (2000).

[29] See Supplemental Material at http://link.aps.org/supplemental/10.1103/PhysRevLett.131.025101 for (i) details of RMHD simulation results on evolution of target plasma density and temperature, (ii) an introduction to the MCNRC code which we developed for Monte Carlo simulations, and (iii) a detailed discussion on scaling of neutron yield with laser intensity in our scheme, which includes Refs. [18,23,30–47].

[30] J. F. Ziegler, M. D. Ziegler, and J. P. Biersack, Nucl. Instrum. Methods Phys. Res., Sect. B **268,** 1818 (2010).

[31] H. W. Lewis, Phys. Rev. **78,** 526 (1950).

[32] M. B. Chadwick et al., Nucl. Data Sheets **112,** 2887 (2011).

[33] S. P. Simakov et al., J. Nucl. Mater. **307,** 1710 (2002).

[34] S. Nakayama et al., J. Nucl. Sci. Tech. **58,** 805 (2021).

[35] D. A. Brown, M. Chadwick, R. Capote et al., Nucl. Data Sheets **148,** 1 (2018).

[36] A. J. Koning, D. Rochman, J. Sublet, N. Dzysiuk, M. Fleming, and S. van der Marck, Nucl. Data Sheets **155,** 1 (2019).

[37] Z. Y. Liu, K. Li, Y. L. Yao, Z. Lei, C. T. Zhou, S. P. Zhu, X. T. He, and B. Qiao, Plasma Phys. Controlled Fusion **63,** 125030 (2021).

[38] J. Fuchs et al., Nat. Phys. **2,** 48 (2006).

[39] B. Qiao, X. F. Shen, H. He, Y. Xie, H. Zhang, C. T. Zhou, S. P. Zhu, and X. T. He, Plasma Phys. Controlled Fusion **61,** 014039. (2019).

[40] X. F. Shen B. Qiao, A. Pukhov, S. Kar, S. P. Zhu, M. Borghesi, and X. T. He, Phys. Rev. E **104,** 025210 (2021).

[41] F. Mirani, A. Maffini, and M. Passoni, Phys. Rev. Appl. **19,** 044020 (2023).

[42] A. Yogo, Z. Lan, Y. Arikawa, Y. Abe, S. R. Mirfayzi et al., Phys. Rev. X **13,** 011011 (2023).

[43] L. Willingale et al., Phys. Plasmas **18,** 083106 (2011).

[44] J. Davis, G. M. Petrov, Tz. Petrova, L. Willingale, A. Maksimchuk, and K. Krushelnick, Plasma Phys. Controlled Fusion **52,** 045015 (2010).

[45] S. P. Simakov, U. Fischer, and P. Pereslavtsev, Fusion Eng. Des. **84,** 1770 (2009).

[46] Aslam, W. V. Prestwich, and F. E. McNeill, Appl. Radiat. Isot. **58,** 321 (2003).

[47] H. Takeshita et al., EPJ Web Conf. **239,** 01018 (2020).

[48] T. Arber, K. Bennett, C. Brady, A. Lawrence-Douglas, M. Ramsay, N. Sircombe, P. Gillies, R. Evans, H. Schmitz, A. Bell et al., Plasma Phys. Controlled Fusion **57,** 113001 (2015).

[49] A. Stockem, E. Boella, F. Fiuza, and L. O. Silva, Phys. Rev. E **87,** 043116 (2013).

[50] K. Xiao, C. Zhou, K. Jiang, Y. Yang, R. Li, H. Zhang, B. Qiao, T. Huang, J. Cao, T. Cai et al., Phys. Plasmas **25,** 023103 (2018).